Available online at www.sciencedirect.com
SCIENCE DIRECT®
Medical Image Analysis 9 (2005) 179–190
MEDICAL IMAGE ANALYSIS
www.elsevier.com/locate/media

Luminosity and contrast normalization in retinal images

Marco Foracchia [1], Enrico Grisan, Alfredo Ruggeri *

Department of Information Engineering, University of Padova, Via Gradenigo 6/a, 35131 Padova, Italy

Received 5 September 2003; received in revised form 24 June 2004; accepted 21 July 2004
Available online 15 September 2004

Abstract

Retinal images are routinely acquired and assessed to provide diagnostic evidence for many important diseases, e.g. diabetes or hypertension. Because of the acquisition process, very often these images are non-uniformly illuminated and exhibit local luminosity and contrast variability. This problem may seriously affect the diagnostic process and its outcome, especially if an automatic computer-based procedure is used to derive diagnostic parameters. We propose here a new method to normalize luminosity and contrast in retinal images, both intra- and inter-image. The method is based on the estimation of the luminosity and contrast variability in the background part of the image and the subsequent compensation of this variability in the whole image. The application of this method on 33 fundus images showed an average 19% (max. 45%) reduction of luminosity variability and an average 34% (max. 85%) increment of image contrast, with a remarkable improvement, e.g., over low-pass correction. The proposed image normalization technique will definitely improve automatic fundus images analysis but will also be very useful to eye specialists in their visual examination of retinal images.
© 2004 Elsevier B.V. All rights reserved.

Keywords: Luminosity; Normalization; Background correction; Low-pass correction; Retinal imaging

1. Introduction

The evaluation of retinal images is a diagnostic tool widely used to gather important clinical information about patient retinopathy. Retinal lesions, related both to vascular aspects, such as increased vessel tortuosity (Hart et al., 1999; Heneghan et al., 2002) or focal/generalized narrowing (Hubbard et al., 1999), and to non-vascular features, such as haemorrhages, exudates, microaneurysms and others (Ege et al., 2000), are important indicators of serious systemic diseases, such as diabetes or hypertension/sclerosis. It is thus very important for the eye specialist to be able to clearly detect and appreciate the lesions present in the image. Retinal images are acquired with a fundus camera, which records, on film or digital sensors such as CCD, the illumination light reflected by the retinal surface. Very often these images are unevenly or non-uniformly illuminated and thus local luminosity and contrast variability are present (Fig. 1). This problem may seriously affect the diagnostic process and its outcome, since lesions in some areas may become hardly visible to a human observer.

Automatic computer-based methods are now often proposed to assist the eye specialist by deriving some parameters from the image, e.g. computing vessel tortuosity or detecting haemorrhages (Ege et al., 2000). Images with large luminosity and contrast variability, both intra- and inter-image, are very difficult to analyze with such automatic systems and the obtained results may be of poor quality. In this case, the normalization step is a necessary pre-requisite, aimed at obtaining images with a common standardized value for luminosity and contrast.

* Corresponding author.
E-mail address: alfredo.ruggeri@unipd.it (A. Ruggeri).
[1] MF is now with M^2 Scientific Computing, Italy.

1361-8415/$ - see front matter © 2004 Elsevier B.V. All rights reserved.
doi:10.1016/j.media.2004.07.001

Fig. 1. Example of observed retinal image.

Several techniques have been used to improve non-uniform luminosity and contrast levels. The classic ones try to normalize image luminosity by disposing of low-frequency luminosity drifts by means of high-pass filtering (Gonzalez and Woods, 2002; Dhawan, 2003), or by approximating the drift with some mathematical function and then subtracting this component from the observed image (Gonzalez and Woods, 2002; Ruggeri and Pajaro, 2002). More complex, space-variant filtering schemes have been proposed to enhance image appearance, with particular regard to locally adaptive contrast enhancement (Wallis, 1976). Other techniques have been proposed for the specific application to retinal images. Background normalization was applied by using a large median filter to extract slow variations of luminosity, which were then subtracted from the observed image (Øien and Osnes, 1995); a brightness adjustment procedure, based on a non-linear point transformation, was also proposed (Wang et al., 2000). Finally, a different approach was proposed in (Wang et al., 2001), which exploited the extraction of vessel pixels, the estimation of the illumination function drift in these pixels, and its subtraction from the observed image.

The main reason that calls for the development of a new and different normalization algorithm is the possible presence in the fundus of many features, e.g., optic disc or various types of lesions, whose visibility has to be preserved and hopefully improved by the normalization process. The approaches that estimate the correction from the whole image will fail in distinguishing luminosity variations due to the presence of these features from variations due to changes in illumination. The result will be a generalized smoothing of image luminosity variations. Locally adaptive non-linear filters (Wallis, 1976), even if capable of producing a better local contrast, still decrease the global difference between bright and dark features and do not guarantee the reduction of luminosity variation throughout the image. The method proposed in (Wang et al., 2001), is a first attempt to overcome these problems, although the choice of vessels as descriptors of luminosity variation has some serious drawbacks. First, vessels are not evenly distributed throughout the image, and the macula region has no vessels at all: this will lead to a very sparse data set to be interpolated to obtain an estimate of the illumination drift. Second, there is a large variability in reflectance between arteries and veins, with vessels showing distinctive luminosity patterns (Denninghoff and Smith, 2000; Li et al., 2003) that make very difficult to reliably estimate and interpolate luminosity drifts.

We propose here a new method to normalize both luminosity and contrast in retinal images, based on a model of the observed image. Luminosity and contrast variability in the background part of the image is estimated and then used for the normalization of the whole image. Normalization is performed both within and between images. Even if it has been developed specifically for retinal images, the proposed technique can be applied to any non-uniformly illuminated image where a background portion is present.

2. Materials and methods

A set of 33 images have been studied, the majority of which show relevant luminosity and contrast drifts. The set included 18 pathological images, presenting visible lesions of various degree. The images were captured with a commercial fundus camera on color film at 50° field of view; the slides were then digitally scanned with a resolution of 1360 dpi, resulting in 1500×1700 pixel images, with 24 bits per pixel. The correction system was designed using the green channel, whose pixel intensities have been normalized to the [0–1] interval, with mean luminosity of the images in the range [0.128, 0.508].

2.1. The model

The luminosity and contrast correction system we propose is based on the following model of the observed fundus image I:

$$I = f(I^{o}) = f\left(I_{b}^{o} + I_{f}^{o}\right), \tag{1}$$

where I^{o} is the original image, I_{b}^{o} is the (original) *background image*, I_{f}^{o} is the (original) *foreground image*, and function $f(\cdot)$ represents the acquisition transformation.

The background image I_{b}^{o} is the ideal image of a retinal fundus free of any vascular structure or visible lesion. The vascular structures, the optic disc and any visible lesion are modelled as an additive term I_{f}^{o} to the background image.

It is rather difficult to express properties of I_{f}^{o}, due to the wide variability of retinal features and lesions that can be found in a fundus image. The only assumption

made regarding I_f^o is that the set of pixels not covered by vascular structures, optic disc or lesions, called the background set $\mathscr{B}$, is not empty.

On the other hand, I_b^o can be statistically modelled as

$$I_b^o(x,y) \sim \mathcal{N}(\mu_b, \sigma_b), \tag{2}$$

i.e., as a white (independence between pixels is assumed) random field with mean value μ_b, representing the ideally uniform luminosity value, and standard deviation σ_b, representing the natural variability of retinal fundus pigmentation. This model can be further simplified by imposing $\mu_b = 0$ and $\sigma_b = 1$; this latter assumption is acceptable as any bias or amplification can be arbitrarily lumped into the luminosity and contrast drifts introduced by the acquisition function.

The acquisition model $f(\cdot)$ describes the contrast and luminosity distortions introduced by the image observation process. Non-uniform contrast and luminosity within an image can be described as

$$I(x,y) = f(I^o(x,y)) = C(x,y)I^o(x,y) + L(x,y), \tag{3}$$

where $C(x,y)$ is the contrast drift factor and $L(x,y)$ is the luminosity drift term. Both contrast and luminosity drifts are space-dependent scalar functions and can therefore be considered as images themselves.

The recovery of an estimate $\hat{I}^o$ of original image I^o is based on the estimation of C and L ($\hat{C}$ and $\hat{L}$), and the compensation of the observed image I as

$$\hat{I}^o(x,y) = \frac{I(x,y) - \hat{L}(x,y)}{\hat{C}(x,y)}. \tag{4}$$

Note that the acquisition model just described does not take into account any blurring or additive noise. The goal of our system is not, in fact, the restoration of the image; therefore we implicitly assume that blurring and noise are already present in the original image I^o we are trying to recover. The resulting normalized image can then be processed by any restoration algorithm.

$C(x,y)$ is assumed to be positive. Both $C(x,y)$ and $L(x,y)$ are assumed to have a spectral content concentrated in the low frequencies, which means that illumination irregularities do not to present rapid changes. This is reasonable for regular fundus imaging techniques that adopt diffused light.

Estimation of drift images can be achieved by considering their effects on the background component of observed image. By combining (3) with (1) we obtain

$$\begin{aligned} I(x,y) &= C(x,y)I^o(x,y) + L(x,y) \\ &= C(x,y)\left[I_b^o(x,y) + I_f^o(x,y)\right] + L(x,y) \\ &= C(x,y)I_b^o(x,y) + C(x,y)I_f^o(x,y) + L(x,y). \end{aligned} \tag{5}$$

If we restrict our analysis to background set $\mathscr{B}$, this expression simplifies to

$$I(x,y) = C(x,y)I_b^o(x,y) + L(x,y), \quad (x,y) \in \mathscr{B}, \tag{6}$$

since by definition $I_f^o = 0$ in $\mathscr{B}$. Using the statistical model of I_b^o (2) and its further simplification, the statistical description of background pixels is

$$I(x,y) \sim \mathcal{N}(L(x,y), C(x,y)), \quad (x,y) \in \mathscr{B}. \tag{7}$$

In summary, the proposed method derives estimates $\hat{L}$ and $\hat{C}$ from the background component of the observed image ($I(x,y), (x,y) \in \mathscr{B}$) by estimating mean and standard deviation of (7), and uses them to recover an estimate $\hat{I}^o$ of the observed image I^o by applying (4).

2.2. Extraction of background pixels

The estimation of C and L requires the preliminary extraction of the background set $\mathscr{B}$. To achieve this goal, the following assumptions have been made: for any pixel of the image, in a neighborhood N of appropriate size s:

(1) both L and C are constant;
(2) at least 50% of the pixels are background pixels;
(3) all background pixels have intensity values significantly different from those of foreground pixels.

The first assumption comes directly from the model hypothesis that the spectral content of L and C is concentrated in the low frequencies, whereas the second one indicates that a sufficient portion of background area must be present in each N. The third assumption allows to determine whether pixels belong to background or not simply by examining their intensity, i.e., any two pixels in N having the same intensity both belong either to background or to foreground.

For each pixel (x,y) in the image, mean $\mu_N(x,y)$ and standard deviation $\sigma_N(x,y)$ of the statistical distribution of intensities in N are estimated. As estimator $\hat{\mu}_N$ for $\mu_N(x,y)$ we used the sample mean; $\hat{\sigma}_N$, estimator for $\sigma_N(x,y)$, was the sample standard deviation. Pixel (x,y) is considered to belong to the background set $\mathscr{B}$ if its intensity is close to the mean intensity in N. This is mathematically expressed by saying that (x,y) belongs to $\mathscr{B}$ if its Mahalanobis distance from $\hat{\mu}_N$, d_M, defined as

$$d_M = \left|\frac{I(x,y) - \hat{\mu}_N}{\hat{\sigma}_N}\right| \tag{8}$$

is lower than a given threshold t.

The procedure for background pixel extraction could be implemented by means of two filters, evaluating $\hat{\mu}_N(x,y)$ and $\hat{\sigma}_N(x,y)$, respectively, for each pixel (x,y). The resulting images could then be combined to evaluate the Mahalanobis distance image, which could be segmented with threshold t to identify the background pixels.

In order to reduce the computational burden, a different implementation has been chosen. The image was partitioned into a tessellation of squares S_i of side s.

For each S_i, $\hat{\mu}(S_i)$ and $\hat{\sigma}(S_i)$ were computed and represented as images. They are a sub-sampled version of the full images $\hat{\mu}_N(x,y)$ and $\hat{\sigma}_N(x,y)$ that would have been obtained with filtering. These full images were then approximated by means of a bicubic interpolation from the sub-sampled images $\hat{\mu}(S_i)$ and $\hat{\sigma}(S_i)$ respectively.

The choice of the value for square side s is critical, since it must satisfy both the assumption on the low spatial dynamics of C and L and the one about the inclusion in S_i of a sufficiently high number of background pixels. In our set of images, a value of $s = 200$ pixels has been empirically chosen, based on a visual inspection of the results.

As regards threshold t, its value was set to 1, which means that, with normally distributed luminosity, about 68% of the square pixels are retained as background (note that Mahalanobis distance is by definition normalized for each pixel by its standard deviation $\hat{\sigma}_N(x,y)$). If all or most of the pixels in the square were background pixels, this choice might lead to some underestimation of background mean luminosity and contrast. This is however very rarely the case; in addition, our aim is the estimation of luminosity and contrast variations and thus, being the procedure the same for all squares, they are not significantly affected.

An example of a background image is shown in Fig. 2 (top panel).

2.3. Estimation of luminosity and contrast drifts

Given the set of background pixels $\mathscr{B}$, $\hat{L}(x,y)$ and $\hat{C}(x,y)$ were derived for each pixel. From (7) and under the first assumption (constant L and C in neighborhood N), background pixel intensities in each N are independent, identically distributed random variables. Thus, $\hat{L}(x,y)$ and $\hat{C}(x,y)$ could be derived for each pixel by estimating mean value and standard deviation of this distribution in N.

This approach has to cope with the same computational problems mentioned in the previous section. Moreover, we are now dealing with a sparse set of pixels (background pixels are only a subset of all image pixels), which renders the application of filtering more difficult. A square-processing solution similar to the one presented in the previous section has been adopted. The image was divided into the same tessellation of squares S_i, and from the set of background pixels $\mathscr{B}$ in S_i, mean and standard deviation of intensity values were estimated by using sample mean and standard deviation estimators. Full $\hat{L}(x,y)$ and $\hat{C}(x,y)$ were then obtained by applying a bicubic interpolation on the sub-sampled images. Examples of computed $\hat{L}(x,y)$ and $\hat{C}(x,y)$ images are shown in Fig. 2 (middle and bottom panels).

The normalized image $\hat{I}^{\circ}$, estimate of observed image I°, was eventually obtained by applying the point transformation (4) to each pixel of the image.

2.4. Color image normalization

Normalization of RGB color images can be performed by independently normalizing each color channel with the above procedure:

$$\begin{pmatrix} \hat{R}^{\circ}(x,y) \\ \hat{G}^{\circ}(x,y) \\ \hat{B}^{\circ}(x,y) \end{pmatrix} = \begin{pmatrix} \frac{1}{\hat{C}_R(x,y)} & 0 & 0 \\ 0 & \frac{1}{\hat{C}_G(x,y)} & 0 \\ 0 & 0 & \frac{1}{\hat{C}_B(x,y)} \end{pmatrix} \times \left[\begin{pmatrix} R(x,y) \\ G(x,y) \\ B(x,y) \end{pmatrix} - \begin{pmatrix} \hat{L}_R(x,y) \\ \hat{L}_G(x,y) \\ \hat{L}_B(x,y) \end{pmatrix} \right]. \tag{9}$$

Being the two factors in this equation orthogonal, norm of differences between vectors are still meaningful (i.e., if the distance between vector a and b is different from zero, the distance between $\hat{a}^{\circ}$ and $\hat{b}^{\circ}$ will still be different from zero). Independent normalization of color components does not however maintain chromatic information. A recovery of the original chromatic distribution can be achieved by identifying an overall image chromatic statistical distribution in the observed image, given by the vectors of sample mean $[\mu_R \mu_G \mu_B]$ and sample standard deviation $[\sigma_R \sigma_G \sigma_B]$, and by forcing it on the normalized image:

$$\begin{pmatrix} \hat{R}_c^{\circ}(x,y) \\ \hat{G}_c^{\circ}(x,y) \\ \hat{B}_c^{\circ}(x,y) \end{pmatrix} = \begin{pmatrix} \sigma_R & 0 & 0 \\ 0 & \sigma_G & 0 \\ 0 & 0 & \sigma_B \end{pmatrix} \begin{pmatrix} \hat{R}^{\circ}(x,y) \\ \hat{G}^{\circ}(x,y) \\ \hat{B}^{\circ}(x,y) \end{pmatrix} + \begin{pmatrix} \mu_R \\ \mu_G \\ \mu_B \end{pmatrix}, \tag{10}$$

where $[\hat{R}_c^{\circ}\ \hat{G}_c^{\circ}\ \hat{B}_c^{\circ}]$ represents the vector of image components normalized with respect to luminosity, contrast and chromatic distribution.

It should be observed, however, that this last step, aimed at maintaining the image overall chromatic statistical distribution, was included to provide images that look more natural when observed by a human expert, but has no influence nor importance on the automatic analysis of images, which is performed on separate color channels.

3. Results

In order to better appreciate the results obtained with the proposed technique, results on both local and global indexes are reported. Using the green channel layer, each test image was partitioned into 25 blocks, 300×340 pixel each, and the results are presented first at block level (local) and then for the whole image (global).

Comparing distribution of local luminosity and contrast between two images, e.g. before and after normalization, is meaningful only if the two images are

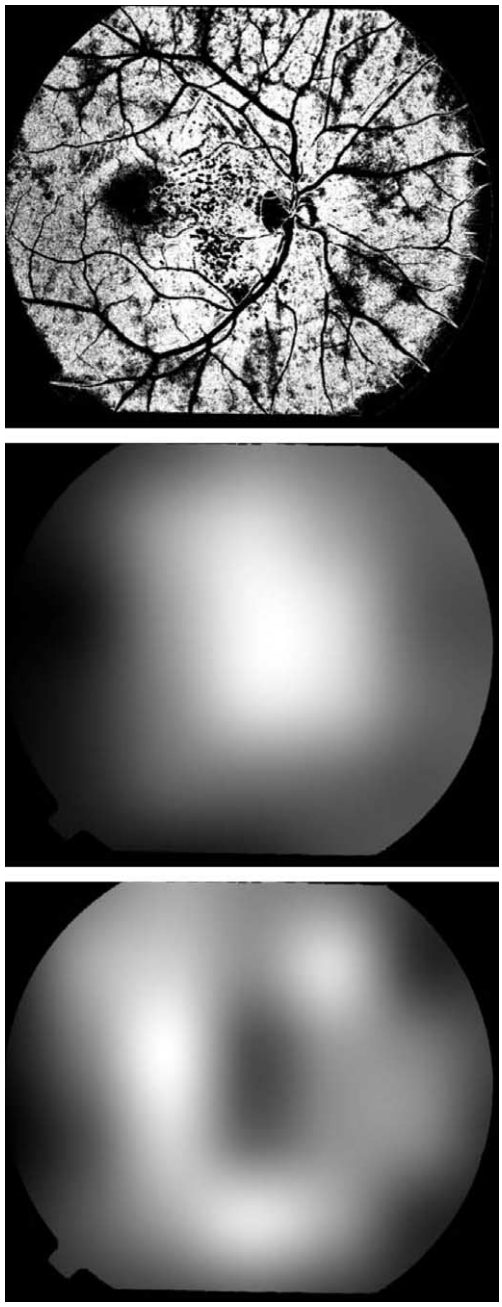

Fig. 2. Computed images: estimated background image (top, white pixels); estimated illumination drift $\hat{L}$ (middle); estimated contrast drift $\hat{C}$ (bottom).

normalized to the same global luminosity and contrast level. In fact, if we compare local distributions between two images having a systematic difference in global luminosity and contrast, the difference between the two local distributions would be affected both by the systematic difference and by the actual difference in local distribution. Let us define $\mu(I)$ as the mean value (luminosity) and $\sigma(I)$ as the standard deviation (contrast) of intensity levels for image I. These two indicators can be arbitrarily modified by means of a linear point transformation on I, e.g., if the transformed image is $I^T = aI + b$ we obtain

$$\mu(I^T) = \mu(aI + b) = a\mu(I) + b, \tag{11}$$

$$\sigma(I^T) = \sigma(aI + b) = a\sigma(I). \tag{12}$$

Before computing performance indexes, our observed and normalized images have been transformed by (11) and (12) so as to have histograms with the same mean and standard deviation. This way, the improvement in luminosity and contrast are not simply due to histogram shift and stretching.

3.1. Local indexes

In order to quantitatively assess the effect of the applied normalization, indexes of luminosity and contrast have been defined and evaluated for each block of the image. The analysis of the distribution of these local indicators over the image allows to express the spatial variation in luminosity and contrast.

For the ith block, luminosity was defined as the mean intensity level, μ_i. Contrast has been quantified by means of two indexes. The first one is based on the standard deviation of intensity levels, σ_i. Since this quantity might be influenced by the presence of locally variable (non-spatially stationary) noise, an additional, theoretically more robust index was defined, based on the distance between 10% and 90% quantile values, $c_i = \text{rank}_{90\%} - \text{rank}_{10\%}$. Both contrast indexes were evaluated only for blocks of the image containing a significant signal, corresponding to portions of the image containing a foreground part (vascular structures or lesions).

The normalization performed by the proposed algorithm provides a uniform luminosity and contrast throughout the image. It modifies local histograms, as can be seen in Fig. 3, where the histograms for the 25 image blocks are shown for the observed and normalized version of the same image. The applied normalization aligns the histogram mean value (luminosity) much closer to the center of the range, and spread them (contrast) over the full range of luminosity values. Normalizing image luminosity has thus a beneficial effect on the local contrast (inside single blocks), even if mean luminosity and contrast were forced to be the same in the normalized and in the observed images. This can be explained by considering that in the observed image a significant portion of the intensity range may be taken up by the luminosity drift, i.e., most of the contrast present in the observed image is due to the difference in mean intensity between different areas of the image. It can be shown that the distribution of intensity values in the union of the two regions, a and b (see Fig. 4), has the following standard deviation (overall contrast):

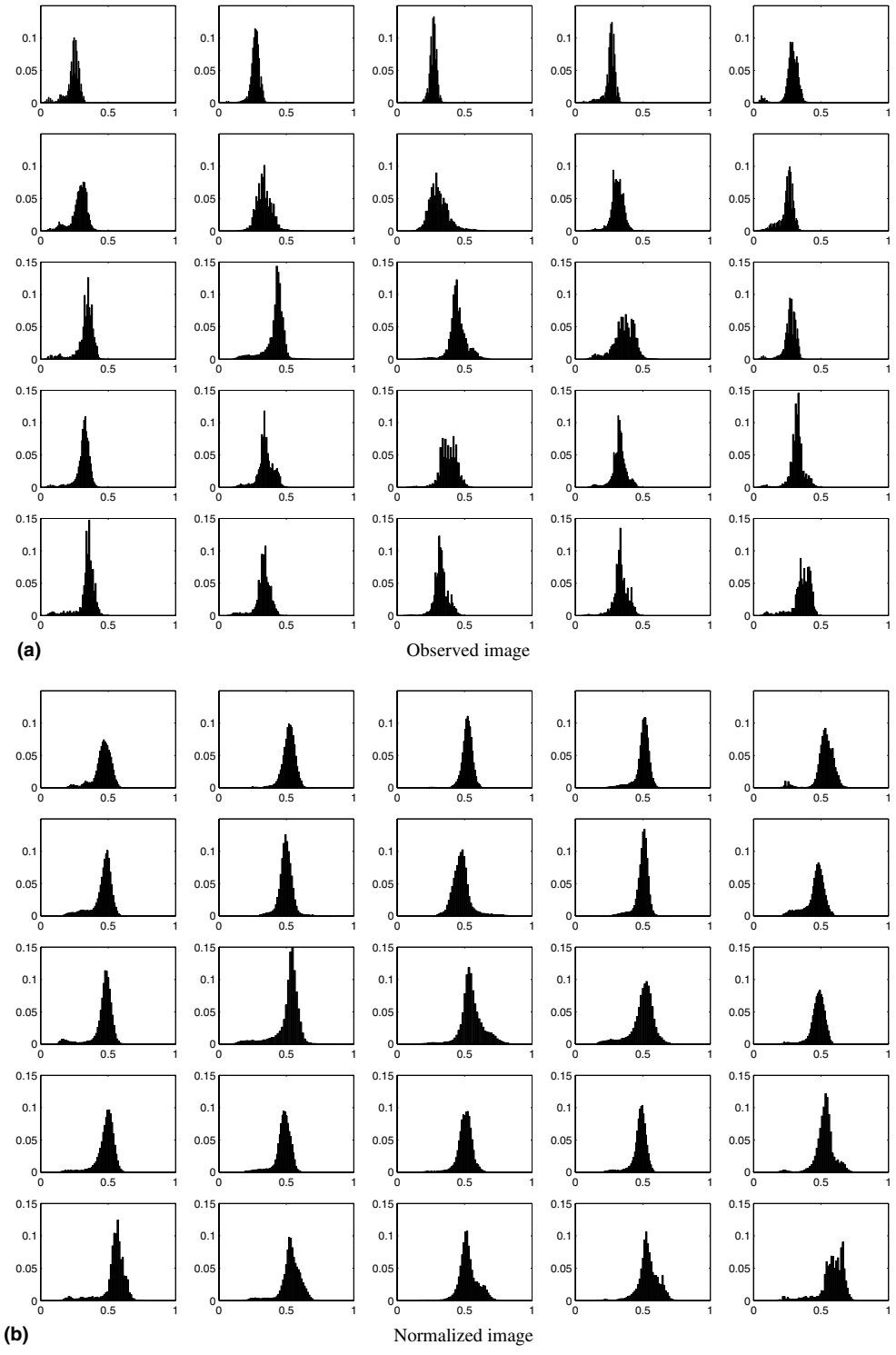

Fig. 3. Histograms of luminosity values in the 25 image blocks for the observed (a) and normalized (b) version of the same image.

$$\sigma_{a\cup b} = \sqrt{\frac{1}{2}\left[\sigma_a^2 + \sigma_b^2 + \frac{1}{2}(\mu_a - \mu_b)^2\right]}. \quad (13)$$

Reducing the difference $(\mu_a - \mu_b)$ clearly increases the sum of the local contrasts, σ_a^2 and σ_b^2, if $\sigma_{a\cup b}$ is kept constant.

3.2. Global indexes

The following indexes were defined for the whole image:

- $\sigma_\mu = \sqrt{\frac{1}{N}\sum_i (\mu_i - \mu_\mu)^2}$, where $\mu_\mu = \frac{1}{N}\sum_i \mu_i$,

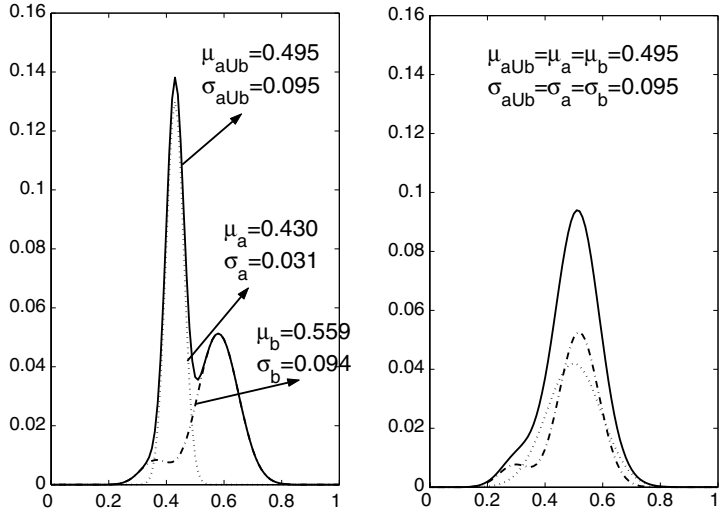

Fig. 4. Enhancement of block contrast by applying luminosity and contrast normalization.

Table 1
Indexes for local luminosity and contrast for observed (σ_μ, μ_σ, μ_c) and normalized (σ_μ^N, μ_σ^N, μ_c^N) images, and their percent differences

	σ_μ	σ_μ^N	% difference	μ_σ	μ_σ^N	% difference	μ_c	μ_c^N	% difference
1	0.037	0.041	12	0.035	0.034	−5	0.085	0.079	−6
2	0.058	0.062	6	0.042	0.039	−6	0.105	0.098	−6
3	0.025	0.019	−21	0.033	0.034	4	0.085	0.087	2
4	0.051	0.031	−38	0.059	0.074	24	0.135	0.160	19
5	0.038	0.038	−1	0.036	0.043	17	0.095	0.110	16
6	0.058	0.043	−25	0.054	0.069	28	0.126	0.158	25
7	0.077	0.068	−11	0.039	0.057	45	0.094	0.134	42
8	0.074	0.060	−20	0.037	0.066	81	0.089	0.161	80
9	0.082	0.071	−14	0.042	0.060	45	0.103	0.149	45
10	0.182	0.197	8	0.070	0.125	80	0.176	0.314	78
11	0.029	0.026	−11	0.032	0.035	10	0.080	0.087	9
12	0.032	0.023	−28	0.030	0.034	13	0.077	0.086	12
13	0.043	0.031	−28	0.036	0.045	26	0.089	0.112	25
14	0.042	0.024	−43	0.035	0.043	22	0.092	0.111	21
15	0.041	0.035	−14	0.035	0.046	33	0.089	0.116	31
16	0.036	0.028	−21	0.034	0.039	15	0.088	0.100	14
17	0.040	0.029	−28	0.034	0.045	32	0.087	0.114	31
18	0.056	0.041	−28	0.043	0.056	32	0.108	0.141	31
19	0.096	0.053	−45	0.051	0.094	85	0.127	0.229	80
20	0.108	0.072	−34	0.055	0.094	70	0.134	0.219	64
21	0.089	0.067	−25	0.053	0.072	35	0.129	0.168	30
22	0.089	0.091	2	0.051	0.089	73	0.108	0.183	70
23	0.061	0.036	−41	0.052	0.075	44	0.118	0.165	40
24	0.078	0.058	−27	0.050	0.070	40	0.112	0.151	34
25	0.062	0.057	−9	0.045	0.057	26	0.095	0.112	18
26	0.090	0.091	1	0.034	0.048	42	0.080	0.111	40
27	0.066	0.048	−27	0.060	0.071	19	0.130	0.156	20
28	0.090	0.059	−34	0.065	0.094	44	0.148	0.202	37
29	0.066	0.052	−20	0.061	0.079	30	0.139	0.175	26
30	0.061	0.050	−17	0.042	0.050	20	0.088	0.103	17
31	0.087	0.060	−31	0.059	0.089	51	0.139	0.203	46
32	0.082	0.066	−20	0.036	0.056	53	0.086	0.128	48
33	0.072	0.071	−2	0.041	0.041	2	0.091	0.088	−3
Average			−19			34			31

- $\mu_\sigma = \frac{1}{N}\sum_i \sigma_i$,
- $\mu_c = \frac{1}{N}\sum_i c_i$,

where $N = 25$ is the number of blocks in the image.

Index σ_μ expresses the variability of the local luminosity throughout the image, and thus the lower this index,

the more uniform the image luminosity. Indexes μ_σ and μ_c express the mean contrast level within the image.

The values of these indexes, evaluated on the set of 33 images, are reported in Table 1. The decrease in standard deviation of local luminosity ranges from −2% to −45%, with an average of −19%; in five images (out of 33), increments were obtained, albeit modest ones (range 1–12%). The mean contrast level μ_σ increases from a minimum of 2% up to 85%, with an average of 34%, and with only two instances of decrement (−5% and −6%); contrast index μ_c showed increments in the range 2–80% (average 31%), with three instances of increment (range −3% to −6%). Fig. 5 (middle panel) shows the result obtained by this technique on a representative image.

3.3. Comparison with other correction techniques

As already mentioned, luminosity and contrast normalization can be achieved also by means of other correction techniques. The low-pass correction, e.g., is obtained by subtracting a low-pass filtered version of the image from the observed image. The procedure proposed in (Wang et al., 2000) performs a pixelwise nonlinear filtering, while the Wallis filter is based on a nonlinear and space-variant technique. At variance with these methods, the technique proposed in (Wang et al., 2001) works only over the vascular part to gather information about luminosity and contrast drift.

In order to allow a better appreciation of the performances of our technique with respect to the others, we have implemented all the above mentioned techniques and compared them with the proposed method. The low-pass filter was implemented by means of a convolution with a Gaussian kernel, whose 3σ value has been set to the square size s of our normalization system. The Wallis filter was implemented as described in an on-line reference (http://www.microimages.com/fetupd/v55/wallis), while the other two techniques have been implemented according to the cited references. For the computation of the local mean and standard deviation, required by the Wallis filter, we have used the values obtained by our first stage (estimation of background pixels), since this method is very similar to the partitioning–interpolating scheme proposed in the cited reference.

The results of these comparisons are presented in Table 2, as regards local luminosity, and in Table 3, as regards contrast (results for the second contrast index, μ_c, are not shown since they are very similar to the ones obtained with the first contrast index, μ_σ). With respect to the proposed technique, image luminosity variability of all other techniques is on average higher (from 11% of the filter proposed by Y. Wang to 40% of low-pass filter), while achieved mean contrast is on average lower (from −3% of the Wallis filter to −28% of the filter proposed by Y. Wang). Fig. 5 (bottom panel) reports an example of the results obtained by the low-pass correction technique on a representative image.

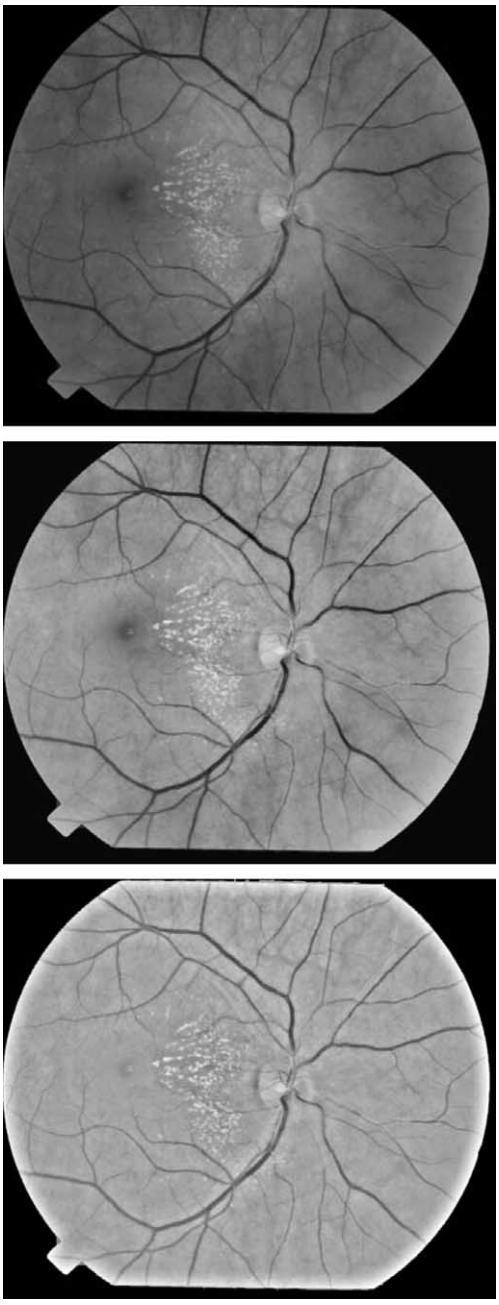

Fig. 5. Results obtained with image normalization techniques. Top: observed image, with luminosity and contrast drifts. Middle: image normalized by the proposed technique. Bottom: image normalized by low-pass correction.

4. Discussion and conclusions

The proposed normalization procedure significantly improves luminosity uniformity and contrast value (Table 1), with significantly better results than the other correction techniques (Tables 2 and 3). The improve-

Table 2
Indexes for local luminosity obtained with the proposed technique (σ_μ^N), the low-pass correction (σ_μ^{LP}), the Wallis filter correction (Wallis, 1976) (σ_μ^W), the correction proposed by H. Wang (Wang et al., 2000) (σ_μ^{HW}), and the correction proposed by Y. Wang (Wang et al., 2001) (σ_μ^{YW})

	σ_μ^N	σ_μ^{LP}	% difference	σ_μ^W	% difference	σ_μ^{HW}	% difference	σ_μ^{YW}	% difference
1	0.041	0.049	18	0.046	11	0.036	−13	0.040	−3
2	0.062	0.067	8	0.064	4	0.058	−6	0.049	−21
3	0.019	0.037	90	0.040	106	0.025	27	0.029	50
4	0.031	0.061	94	0.044	41	0.048	53	0.047	51
5	0.038	0.054	42	0.047	24	0.038	1	0.038	−1
6	0.043	0.069	60	0.058	33	0.057	31	0.045	5
7	0.068	0.068	−1	0.065	−6	0.079	16	0.047	−31
8	0.060	0.071	18	0.077	30	0.077	29	0.052	−13
9	0.071	0.068	−4	0.059	−17	0.085	20	0.056	−20
10	0.197	0.106	−46	0.144	−27	0.196	−1	0.102	−48
11	0.026	0.043	66	0.033	27	0.028	10	0.032	26
12	0.023	0.041	81	0.037	64	0.032	39	0.028	26
13	0.031	0.055	77	0.042	35	0.043	40	0.045	46
14	0.024	0.054	128	0.046	94	0.042	76	0.037	57
15	0.035	0.055	57	0.052	47	0.041	16	0.043	23
16	0.028	0.047	67	0.044	55	0.036	27	0.033	17
17	0.029	0.053	81	0.050	69	0.041	39	0.037	28
18	0.041	0.063	56	0.047	15	0.056	37	0.048	18
19	0.053	0.094	76	0.096	80	0.097	83	0.087	64
20	0.072	0.094	31	0.102	43	0.110	54	0.079	10
21	0.067	0.084	25	0.074	10	0.081	22	0.103	53
22	0.091	0.083	−8	0.081	−11	0.091	0	0.075	−18
23	0.036	0.066	83	0.056	54	0.060	65	0.046	28
24	0.058	0.073	26	0.062	8	0.074	29	0.069	20
25	0.057	0.069	22	0.065	15	0.061	7	0.049	−13
26	0.091	0.087	−4	0.089	−2	0.089	−2	0.065	−28
27	0.048	0.063	30	0.059	23	0.062	28	0.059	23
28	0.059	0.069	17	0.063	6	0.087	47	0.065	10
29	0.052	0.066	26	0.067	28	0.065	23	0.062	18
30	0.050	0.060	21	0.049	−2	0.058	15	0.045	−10
31	0.060	0.079	31	0.059	−1	0.078	30	0.067	11
32	0.066	0.084	27	0.065	−1	0.082	24	0.064	−2
33	0.071	0.076	8	0.076	7	0.070	−1	0.074	5
Average			40		26		26		11

ment can also be appreciated by observing the results shown in Fig. 5 for the proposed technique and the low-pass correction. By comparing the two normalized images, one can note that the low-pass corrected image markedly exhibits a smoothing effect around retinal structures (e.g. vessel or lesion), resulting in a heavily reduced contrast and ringing effects in these areas. This can be explained by considering on a row of pixels the drift corrections proposed by the low-pass filter and by our technique (Fig. 6). The drift estimated by the simple low-pass filter is greatly influenced by the presence of retinal structures, since it incorporates them into the drift used for correction. On the contrary, our normalization system is not affected by this portion of the signal, being based only on the background part of the image, and thus its drift correction does not smooth vessels or lesions. The effect of this can also be seen in the macula (the darker area on the left-hand side in Fig. 5, top panel), which is almost invisible in the low-pass corrected image.

This behavior of the low-pass correction is also responsible for the apparently better results it achieved in some images (e.g. no. 10) where it scored significantly better than the proposed technique as regards luminosity variability and contrast. This image contains many pathological areas, which appear as extended bright or dark areas (see e.g. observed image no. 10, shown in Fig. 7, top panel). The low-pass correction considers the predominant grey-level of these areas as the main luminosity value: its correction yields an overall more uniform luminosity, but it also saturates towards zero the background areas surrounded by bright pathological areas. Moreover, when the corrected image was transformed with (11) and (12) so as to have an histogram with the same mean and standard deviation as the observed image, the amplification of the reduced dynamic range of grey levels translates into an increase of the global index for contrast. These better indexes are however obtained at the expenses of a notable image distortion. This is quite evident when one visually examines the

Table 3
Indexes for contrast obtained with the proposed technique (μ_σ^N), the low-pass correction (μ_σ^{LP}), the Wallis filter correction (Wallis, 1976) (μ_σ^W), the correction proposed by H. Wang (Wang et al., 2000) (μ_σ^{HW}), and the correction proposed by Y. Wang (Wang et al., 2001) (μ_σ^{YW})

	μ_σ^N	μ_σ^{LP}	% difference	μ_σ^W	% difference	μ_σ^{HW}	% difference	μ_σ^{YW}	% difference
1	0.034	0.025	−26	0.034	−1	0.037	8	0.021	−39
2	0.039	0.035	−10	0.040	3	0.042	8	0.028	−29
3	0.034	0.020	−40	0.025	−25	0.032	−4	0.014	−57
4	0.074	0.061	−17	0.069	−6	0.063	−15	0.058	−22
5	0.043	0.029	−32	0.040	−6	0.038	−11	0.027	−36
6	0.069	0.058	−16	0.064	−7	0.058	−17	0.060	−14
7	0.057	0.060	6	0.063	12	0.039	−30	0.057	0
8	0.066	0.060	−10	0.064	−3	0.038	−42	0.058	−13
9	0.060	0.065	8	0.072	20	0.043	−28	0.049	−19
10	0.125	0.158	26	0.118	−6	0.073	−42	0.123	−2
11	0.035	0.023	−35	0.031	−11	0.032	−7	0.019	−47
12	0.034	0.020	−42	0.027	−22	0.030	−12	0.020	−42
13	0.045	0.033	−28	0.044	−3	0.037	−18	0.028	−37
14	0.043	0.030	−30	0.035	−18	0.036	−16	0.028	−34
15	0.046	0.032	−31	0.036	−22	0.035	−24	0.025	−45
16	0.039	0.023	−40	0.029	−26	0.034	−14	0.022	−44
17	0.045	0.026	−42	0.032	−29	0.033	−26	0.027	−40
18	0.056	0.040	−29	0.055	−3	0.044	−21	0.035	−37
19	0.094	0.077	−18	0.079	−16	0.051	−46	0.063	−33
20	0.094	0.094	1	0.083	−11	0.058	−38	0.077	−17
21	0.072	0.063	−12	0.081	12	0.056	−22	0.043	−41
22	0.089	0.071	−21	0.071	−20	0.059	−34	0.049	−45
23	0.075	0.057	−23	0.068	−10	0.056	−26	0.051	−32
24	0.070	0.066	−5	0.081	17	0.052	−25	0.058	−17
25	0.057	0.048	−16	0.057	2	0.048	−15	0.046	−18
26	0.048	0.044	−9	0.066	38	0.037	−24	0.035	−27
27	0.071	0.068	−4	0.076	6	0.059	−17	0.059	−17
28	0.094	0.088	−6	0.098	4	0.070	−26	0.082	−13
29	0.079	0.066	−17	0.069	−14	0.063	−20	0.052	−35
30	0.050	0.044	−12	0.055	9	0.041	−18	0.047	−7
31	0.089	0.079	−11	0.099	11	0.065	−27	0.076	−15
32	0.056	0.048	−14	0.063	14	0.036	−36	0.046	−18
33	0.041	0.039	−5	0.045	9	0.044	6	0.030	−27
Average			−17		−3		−21		−28

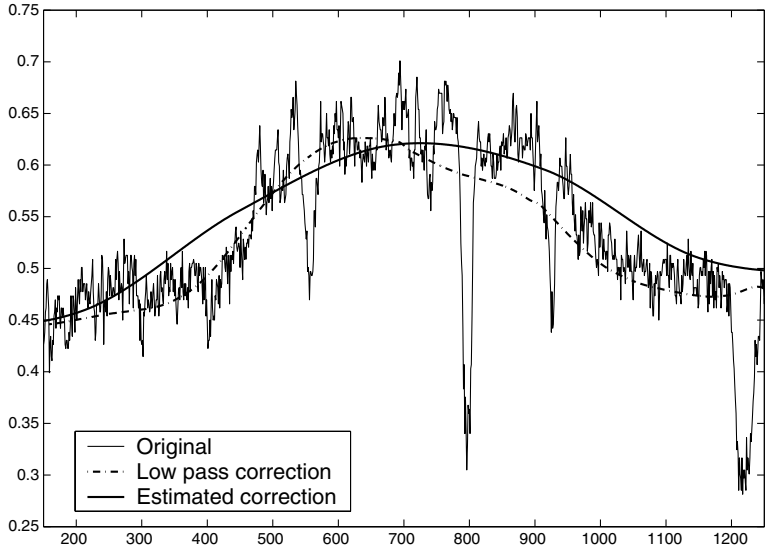

Fig. 6. Intensity profile on a sample row and intensity drift correction estimated by the proposed technique and by a low-pass filter.

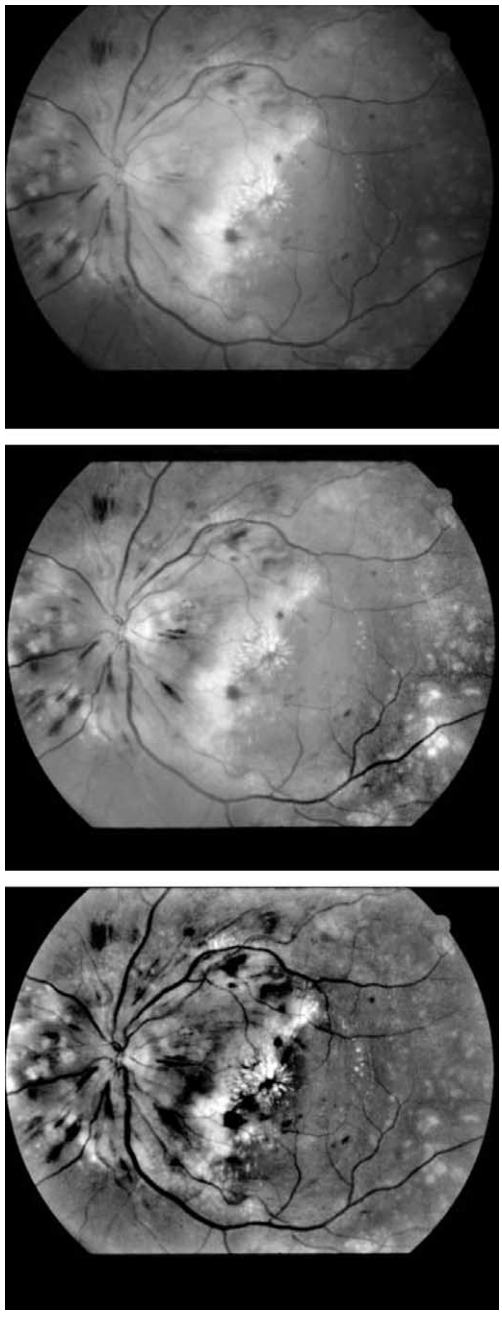

Fig. 7. Results obtained with image normalization techniques on image no. 10. Top: observed image, with many large pathological areas. Middle: image normalized by the proposed technique. Bottom: image normalized by low-pass correction.

images corrected by either techniques, vis-a-vis with the observed image: at variance with the proposed technique (Fig. 7, middle panel), the low-pass correction introduces highly visible and confounding artifacts, such as dark blobs around the optic disk and around other bright areas (Fig. 7, bottom panel).

The normalization method based on the Wallis filter provided good results as regards contrast enhancement, only slightly worse than our proposed procedure, but poor ones for the local luminosity normalization. The method by Y. Wang, on the contrary, scored reasonably well in local luminosity normalization, but failed in contrast enhancement. This latter approach, based on drift estimation from vessels only, is seriously affected by the different reflectance of arteries and veins, which would be erroneously treated as a difference in illumination, and by the questionable extrapolation of the drift, estimated in the surrounding regions, to the rather wide macular area, where no vessels are present.

As regards our proposed algorithm, a possible limitation is given by the hypothesis that at least 50% of the pixels in each square are background pixels. This assumption may not hold in some areas, e.g., macula, papilla or zones with large exudates or laser treatments. In order to reduce as much as possible the number of such instances, we preliminarily removed from the set of squares considered for drift estimation those squares with mean luminosity higher than an empirically determined threshold (0.75 in a 0–1 scale). In this way, zones with papilla or other large bright features, e.g. large exudates, were actually not considered in the drift estimation process (normalization was however applied also to these zones). We could not apply the same removal technique to zones with large dark areas, e.g. macula or large haemorrhages, since their luminosity may be very similar to that of some regions of background (e.g., peripheral zones with weak illumination), and a removal technique would have removed also a fairly large number of background areas. However, the presence of few zones with "non-background" dark areas larger than 50% of the square did not significantly affect the normalization procedure: results on our test images, obtained with manual inclusion/exclusion of these zones, showed with the former only a slightly higher brightness in the central part of these areas.

The algorithm proposed here mainly originated from our needs of obtaining normalized images, to be processed by automatic techniques in order to extract diagnostic information about vascular (Foracchia et al., 2002; Grisan et al., 2003; Foracchia et al., 2004) and non-vascular lesions (Grisan et al., 2001). As such, it greatly improved the performances of these techniques and allowed them to process a much wider range of images. However, these normalized images were also judged quite interesting by eye specialists for their visual examination of the retina, since they made the vessel network and the non vascular lesions, when present, much more visible. A clinical evaluation of this additional application of the proposed technique is currently in progress.

Acknowledgments

This work was supported in part by Nidek Technologies, Italy. Preliminary results were presented at the

3rd International Workshop on Computer Assisted Fundus Image Analysis (CAFIA 3), Turin, Italy, 27–30 March, 2003. The authors thank Dr. S. Piermarocchi, from the Department of Ophthalmology, University of Padova, Italy, Dr. P. Lanzetta, from the Department of Ophthalmology, University of Udine, Italy, and Dr. S. Saviano, from the Ophthalmology Unit, Trieste Hospital, Italy, who provided the fundus images.

References

Denninghoff, K.R., Smith, M.H., 2000. Optical model of the blood in large retinal vessels. J. Biomed. Opt. 5, 371–374.

Dhawan, A.P., 2003. Medical Image Analysis. Wiley–Interscience, New York.

Ege, B.M., Hejlesen, O.K., Larsen, O.V., Møller, K., Jennings, B., Kerr, D., Cavan, D.A., 2000. Screening for diabetic retinopathy using computer based image analysis and statistical classification. Comput. Methods Prog. Biomed. 62, 165–175.

Foracchia, M., Grisan, E., Ruggeri, A., 2002. Detection of vessel caliber irregularities in color retinal fundus images by means of fine tracking. In: Hutten, H., Krösl, P. (Eds.), IFMBE Proc., Vol. 3: EMBEC '02, December, pp. 1558–1559.

Foracchia, M., Grisan, E., Ruggeri, A., 2004. Detection of optic disc in retinal images by means of a geometrical model of vessel structure. IEEE Trans. Med. Imaging, in press.

Gonzalez, R.C., Woods, R.E., 2002. Digital Image Processing. Prentice-Hall, Englewood Cliffs, NJ.

Grisan, E., Foracchia, M., Ruggeri, A., Oct 2001. Detection and classification of nonvascular diagnostic signs in retinopathy fundus images. In: Proc. 2nd International Workshop on Computer Assisted Fundus Image Analysis (CAFIA-2), p. 21.

Grisan, E., Foracchia, M., Ruggeri, A., 2003. A novel method for the automatic evaluation of retinal vessel tortuosity. In: Proc. 25th Annual International Conference of IEEE-EMBS. IEEE, pp. 866–869.

Hart, W.E., Goldbaum, M., Côté, B., Kube, P., Nelson, M.R., 1999. Measurement and classification of retinal vascular tortuosity. Int. J. Med. Inf. 53 (2–3), 239–252.

Heneghan, C., Flynn, J., O'Keefe, M., Cahill, M., 2002. Characterization of changes in blood vessel width and tortuosity in retinopathy of prematurity using image analysis. Med. Image Anal. (6), 407–429.

Hubbard, L., Brothers, R., King, W., Clegg, L., Klein, R., Cooper, L., Sharrett, A., Davis, M., Cai, J., 1999. Methods for evaluation of retinal microvascular abnormalities associated with hypertension/sclerosis in the atherosclerosis risk in communities study. Ophthalmology 106 (12), 2269–2280.

Li, H., Hsu, W., Lee, M., Wang, H., 2003. A piecewise Gaussian model for profiling and differentiating retinal vessels. In: Proc. ICIP'03, Barcelona, September 14–17, pp. 1069–1072.

Øien, G., Osnes, P., September 1995. Diabetic retinopathy: automatic detection of early symptoms from retinal images. In: Proc. NORSIG-95 Norwegian Signal Processing Symposium. Available at http://www.ux.his.no/sigproc/www/norsig/norsig95.html.

Ruggeri, A., Pajaro, S., 2002. Automatic recognition of cell layers in corneal confocal microscopy images. Comput. Methods Prog. Biomed. 68 (1), 24–35.

Wallis, R., 1976. An approach to the space variant restoration and enhancement of images. In: Proc. IEEE Conference on Computer Vision and Pattern, Naval Postgraduate School, Monterey, CA, USA.

Wang, H., Hsu, W., Goh, K.G., Lee, M.L., Jun 2000. An effective approach to detect lesions in color retinal images. In: Proc. IEEE Conference on Computer Vision and Pattern Recognition, vol. 2, pp. 181–186.

Wang, Y., Tan, W., Lee, S., 2001. Illumination normalization of retinal images using sampling and interpolation. In: Sonka, M., Hanson, H. (Eds.), Medical Imaging 2001: Image Processing. Proc. of SPIE, vol. 4322, SPIE, pp. 500–507.